PCCP

Dynamics and thermochemistry of the negatively charged clusters in the 2-hydroxyethylhydrazinium nitrate ionic liquid system

SCHOLARONE™
Manuscripts

Dynamics and thermochemistry of the negatively charged clusters in the 2-hydroxyethylhydrazinium nitrate ionic liquid system

Wenjing Zhou,[a,b] Jianbo Liu,[a,b*] Steven D. Chambreau,[c] and Ghanshyam L. Vaghjiani[d]

[a] Department of Chemistry and Biochemistry, Queens College of the City University of New York, 65-30 Kissena Blvd., Queens, New York 11367, USA;

[b] Ph.D. Program in Chemistry, the Graduate Center of the City University of New York, 365 5th Ave., New York, New York 10016, USA;

[c] Jacobs Technology, Inc., Air Force Research Laboratory, Edwards Air Force Base, California 93524, USA;

[d] In-Space Propulsion Branch, Rocket Propulsion Division, Aerospace Systems Directorate, Air Force Research Laboratory, AFRL/RQRS, Edwards Air Force Base, California 93524, USA

Abstract The formation and fragmentation of the negatively charged 2-hydroxyethylhydrazinium nitrate ($[HOCH_2CH_2NH_2NH_2]^+NO_3^-$, HEHN) ionic liquid clusters were examined using a guided-ion beam tandem mass spectrometer furnished with collision-induced dissociation of selected ions with the Xe atoms. Measurements included the compositions of cluster ions formed in the ionization source, and the dissociation products, cross sections, and 0 K threshold energies for individually selected cluster ions. To identify the structures of the main cluster ion series $[(HEHN)_n(HNO_3)_{0-1}NO_3]^-$ formed, molecular dynamics simulations were employed to create initial geometry guesses, followed by optimization at the ωB97XD/6-31+G(d,p) level of theory, from which global minimum structures were identified for reaction thermodynamics analyses. A comparison was made between the cluster formation and fragmentation in the negatively charged 2-hydroxyethylhydrazinium nitrate with those in the positive mode (reported by Zhou et al.; *Phys. Chem. Chem. Phys.*, 2023, **25**, 17370). In both modes, the cluster ions were predominantly composed of *m/z* below 350; loss of neutral 2-hydroxyethylhydrazinium nitrate ion pair represents the most important cluster fragmentation pathway, followed by intra-ion pair proton transfer-mediated 2-hydroxyethylhydrazine and HNO_3 elimination; and all clusters started to dissociate at threshold energies less than 1.5 eV. The overwhelming similarities in the formation and fragmentation chemistry of positively vs. negatively charged 2-hydroxyethylhydrazinium nitrate clusters may be attributed to their inherent ionic nature and high electric conductivities.

*Corresponding author E-mail: jianbo.liu@qc.cuny.edu. Tel: 1-718-997-3271.

1   Introduction

Ionic liquids (ILs)[1] were first utilized as green solvents for synthesis,[2] catalysis,[2] extraction,[3] and

crystallization.[4] The capability and flexibility in designing, tailoring, and customizing IL chemical and

physical properties for targeted criteria are able to expand their applications to more versatile fields, such

as additives for enhancing reactivity and durability in fuel cells,[5] electrolyte in lithium-ion batteries,[6] CO_2

capture and utilization,[7] gas sensors,[8] hydraulic oils,[9] ion gels,[10] and alternative energy source[11-18] for

propulsion. These applications are based on the reduced toxicity and lower vapor pressure of ILs, as well

as their ionic nature, higher electrical conductivities, and lower viscosities.

The adoption of ILs for various applications has greatly promoted the fundamental research on the IL

thermochemistry and chemical reactions. Many of these works were accomplished via mass

spectrometry,[19-28] since mass spectrometry represents a compelling avenue to explore the mechanisms,

kinetics, and dynamics for the chemical reactions and fragmentation of single IL constituent ions and

ionic clusters, both in the presence and the absence of counter ions.[29] 2-Hydroxyethylhydrazinium

nitrate[30] (abbreviated as HEHN, $[HOCH_2CH_2NH_2NH_2]^+NO_3^-$) is a protic IL, produced by the

stoichiometric neutralization of 2-hydroxyethylhydrazine (HE) with HNO_3. It is a liquid at ambient

temperature with a glass transition temperature of 216.1 K and a melting point of 228 K.[31] There have

been multiple mechanistic studies on the thermal and catalytic decomposition of 2-hydroxyethyl-

hydrazinium nitrate reported in the literature.[30, 32-34] In the perspective of cluster formation, Prince et al.[25]

measured the first mass spectra for the HEHN cluster ions in 2012 and later simulated dissociation

kinetics of $[(HEHN)_{1-3}HE + H]^+$.[35] In 2018, Patrick et al.[28] reported collision-induced dissociation (CID)

of $[(HE)_2 + H]^+$ and $[(HEHN)_2HE + H]^+$. In 2020, Zeng et al.[36] characterized H-bonding motifs in

$[(HEHN)_{1-5}HE + H]^+$. More recently, we completed a combined mass spectrometry and dynamics study

of the formation and dissociation of $[(HEHN)_n(HE)_{1-2} + H]^+$, $[(HE)_{n+1} + H]^+$, and $[(HE)_nC_2H_4OH]^+$ (n =

0–2).[37] Our work demonstrated the formation of extensive cluster ions[38, 39] and nanoclusters,[40] in addition

to single ions, and found that the cluster formation is intimately correlated to in- and after-source cluster

fragmentation.[28, 35, 41-49]

In the present work, we have expanded our investigations to the negatively charged clusters of 2-hydroxyethylhydrazinium nitrate. The motivations are rationalized as follows. ILs consist of cationic and anionic components. During the formation of charged clusters in the gas phase, ions and clusters of a single polarity are extracted from IL. The remaining counterions are accumulated in the liquid, which must be neutralized through electrochemical reactions (otherwise, the extra counterions would build up a field counter to the externally applied ionization field, negatively affecting ion migration in the liquid and ion trajectory in the gas phase[50]). However, electrochemical reactions bring changes in the IL compositions. Alternating the ionization between positive and negative modes can suppress electrochemical reactions.[51, 52] The mechanism behind the bipolar mode is that a double layer structure forms at the electrode-liquid interface due to charge transfer between the electrode and emitted ions. As the voltage alternates, the potential difference across the double layer drops and mitigating electrochemical reactions,[51] rendering the possibility of efficient ion formation.

However, there is a dearth of information on negative IL clusters in the literature.[49, 53, 54] To the best of our knowledge, the present work represents the first paper on the compositions, structures, and reactions of the HEHN clusters in the negative mode. The subsequent sections of this paper are structured as follows. Section 2 provides a concise overview encompassing instrumentation, experimental setup, and data analysis for the measurement of negatively charged ion compositions and kinetic energy-dependent CID of selected cluster ions. Section 3 describes classical molecular dynamics simulations, quasi-classical direct dynamics simulations, and density functional theory (DFT) calculations used in the search of probable cluster structures and dissociation pathways. Section 4 reports the negative mass spectrum of HEHN and the CID of selected primary ions. The negative cluster dissociation behaviors are further discussed and compared to their positive counterparts in Section 5. Conclusions are presented in Section 6.

2   Experimental Section

2.1 MS and MS/MS measurements

Mass spectra were measured on a home-built guided-ion beam tandem mass spectrometer located at CUNY Queens College.[55] Here only a concise description is given focusing on the instrumentation parameters used in this study. The mass spectrometer consists of, in a sequential order, a source chamber that was coupled to an ion source, a hexapole radio-frequency (rf) ion guide, a reactant-selection quadrupole mass filter, an octopole ion guide surrounded by a scattering cell, a product-detection mass filter, and a pulse-counting electron multiplier. A 35-gauge hypodermic stainless steel ion emitter (0.13 mm o.d. × 0.05 mm i.d.) was operating at a voltage of −2.0 to −4.0 kV relative to the ground with a flow rate of 0.06 mL/hour. The HEHN sample was diluted to a concentration of 5 mM. A variety of solvents were tested for negative clusters of HEHN, following the same protocol used for other ILs.[37, 56] An acetonitrile:water 3:1 solution which had previously been chosen for the positive clusters of HEHN[37] yielded the best stability and ion abundance in the negative mode as well. Acetonitrile also prevented corona discharge at the emitter that otherwise would occur in the ionization of pure aqueous solutions.[56-59] No additional pH adjustment was needed.

The charged liquid droplets emitted from the source underwent desolvation as they passed through a heated inlet capillary (in the temperature range of 120 − 180 °C, which was biased between −70 and −180 V relative to the ground) and converted into gaseous ions in the source chamber. A skimmer of 1.0-mm orifice was located at 3 mm away from the end of the capillary. The skimmer was biased at −20 to −60 V relative to the ground. The electrical field between the end of the capillary and skimmer promoted collision induced desolvation of remaining solvent clusters.[60-62] Ions that passed through the skimmer were transported into the hexapole ion guide for collisional energy damping and space focusing,[63-65] through which ions were thermalized to a Boltzmann internal energy distribution at 310 K[55] and tightly focused into the entrance of the first quadrupole mass filter.

For measurement of primary ion compositions, the first quadrupole mass filter operated in a rf ion-guide mode, and all ions were transmitted to the second quadrupole mass filter for mass scan. For measurement of CID tandem MS, ions were mass selected in the first quadrupole mass filter. The

selected ions were focused into the octopole ion guide that passes through the 10-cm scattering cell

wherein the ions underwent CID with the Xe gas (Spectral Gases, 99.95%). The octopole not only

trapped ions in the radial direction using a rf potential but also controlled the kinetic energy of ions in the

laboratory frame (E_{lab}) using a DC bias. The latter set the collision energy (E_{col}) between ions and neutral

target in the center-of-mass (CM) frame via $E_{CM} = E_{lab} \times m_{neutral}/(m_{ion} + m_{neutral})$, where $m_{neutral}$ and m_{ion}

indicate the masses of the neutral atom and ion, respectively. The absolute pressure of Xe gas inside the

scattering cell was maintained at less than 0.04 mTorr and measured using a capacitance manometer. The

low target gas pressure was essential for ensuring, at most, single collisions between ions and the Xe

atoms. This simplified data analysis as we only needed to consider energy transfer for single collision

events. Under single-collision conditions, the kinetic-energy dependent dissociation cross section (σ) was

determined using a thin-target approximation,[66] i.e., $\sigma = k_B T \cdot \frac{I_{product}}{I_{reactant} \times P_{cell} \times l_{cell}}$, where k_B is the

Boltzmann constant, T is the temperature of reactants, P_{cell} is the target gas pressure in the scattering cell,

l_{cell} is the effective cell length, and $I_{reactant}$ and $I_{product}$ are the intensities of reactant ions (when the Xe gas

was not directed into the scattering cell) and product ions (after correcting for background when Xe was

no longer directed into the cell), respectively. The experiment was repeated four times under the same

conditions, from which relative uncertainties were determined.

2.2 Analysis of 0 K dissociation threshold energy (E_0)

E_0 was determined from E_{CM}-dependent product ion cross sections following a line-of-centers (LOC)

model-based analysis:[67-70]

$$\sigma(E_{CM}) = \sigma_0 \frac{(E_{CM} + E_{vib} + E_{rot} - E_0)^n}{E_{col}} \qquad (1)$$

where σ_0 is a normalization factor, E_{CM} and E_0 are as described before, E_{vib} and E_{rot} are the vibrational and

rotational energies of reactant ions, and n is a fitting parameter that determines the energy transfer

efficiency from E_{CM} to E_{vib} and E_{rot}. The hypothesis behind the LOC model is that a fraction of near-

threshold collisions are completely inelastic so that all E_{CM} contributes to overcome E_0, as previously

verified in the threshold CID of various ionic species[69-71] including IL cluster ions.[37, 56]

The energy dependence of experimental $\sigma(E_{CM})$ was broadened by the translational energy

distributions of primary ions and target gas and the internal energy distributions of primary ions.[72, 73] A

Monte Carlo program was used to simulate the experimental energy broadening, including convolution

and fitting.[74, 75] In brief, for each product ion channel at each nominal E_{CM}, the simulation initiated a set

of 100000 ions with Boltzmann distributions of E_{vib} and E_{rot} at the experimental ion temperature 310 K.

Each ion has a translational kinetic energy drawn from a Lorentzian distribution of E_{lab}. The Lorentzian

distribution has a peak value corresponding to the desired E_{CM} and the full-width at half maximum

(fwhm, representing the ion kinetic energy width) of 0.65 eV as determined by a retarding potential scan

on the octopole.[55, 76] The Xe atoms were sampling the translational energy distribution at room

temperature to account for their thermal motion. To take into account kinetic shift[77] in near-threshold

collisions, a Rice-Ramsperger-Kassel-Marcus (RRKM) unimolecular rate model[78] was incorporated into

the fitting to calculate dissociation rates with total available energies. Only the collisions that had led to a

dissociation within the ion time-of-flight (100 to 500 μs depending on E_{CM}) were counted toward $\sigma(E_{CM})$.

The collision outcomes at various E_{CM} were fed into Eqn. (1). A leveling-off function was used to allow

$\sigma(E_{CM})$ to reach a plateau at high energies.

3   Computational Section

3.1 Classical molecular dynamics simulations of ion conformations followed by DFT calculations

Initial guesses for the conformations of cluster ions were created by classical molecular dynamics

simulations using GROMACS.[79, 80] The detailed procedure was described previously.[37] As the neutral

pair of HE·HNO$_3$ does not exist within HEHN cluster ions,[28, 36, 37] only [HE + H]$^+$, NO$_3^-$, and HNO$_3$ were

fed into the simulations as starting constituents. A space of 3 nm × 3 nm × 3 nm was chosen for

simulating cluster ions of $m/z \leq 400$, and that of 4 nm × 4 nm × 4 nm was chosen for larger ions. Hessian

matrices for the constituents were derived from Gaussian 16[81] electronic structure calculations. Universal

force field and topology files were generated using the Sobtop program.[82] An initial energy-minimization

process was carried out under NVT (canonical ensemble of constant temperature and volume). The

identified minimum-energy structure served as the starting point in a series of simulated annealing[83] as follows: the simulation ramped the system temperature from 300 K to 500 K within 3 psec, followed by 4 psec at 500 K for dynamics, and another 3 psec for cooling to 300 K. The resulting candidate structure was used as a starting structure to initiate a new annealing iteration.

Following this sequence, a set of $100 - 200$ candidate structures was created to cover most of the probable conformations for each cluster composition. Their geometries were viewed using the VMD program[84] to remove obvious duplicates. All unique structures were optimized using the ωB97XD functional at several basis sets of increasing size. To remove extremely high-energy conformers, we first used a relatively small basis set 3-21G to identify all the conformers (approximately 50) within a 0.8 eV energy range. These conformers were refined by employing the 6-31G(d) basis set, followed by the 6-31+G(d,p) basis set. The DFT calculations also provided harmonic frequencies to distinguish stationary vs. saddle points, from which low-energy stable structures and global minima were located.

3.2 Validation of ion conformations using quasi-classical, direct dynamics simulations

As a cross-validation of the classical dynamics simulations, the $[(HEHN)NO_3]^-$ cluster was subjected to Born-Oppenheimer direct dynamics trajectory simulations.[85-89] The trajectories followed the formation of $[(HEHN)NO_3]^-$ via collisions of HEHN and NO_3^-. Initial conditions for bimolecular collisions were set up using the Venus program[90, 91] coupled to Gaussian. The potential minima of HEHN (i.e., the neutral pair $HE \cdot HNO_3$) and NO_3^- were calculated at the ωB97XD/6-31+G(d) level of theory. E_{vib} for the normal mode of reactant vibration was selected from a 310 K quantum Boltzmann probability distribution[92] $P(n_i) = \exp(-n_i h\upsilon_i/k_BT)[1 - \exp(-h\upsilon_i/k_BT)]$ where υ_i and n_i are the vibrational frequency and quantum number of the ith mode, respectively; and T is the temperature of the reactant. The resulting normal mode energy, including zero-point energy (ZPE), was partitioned between kinetic and potential energies by choosing a random phase for each mode. E_{rot} of the reactants was sampled from a classical Boltzmann distribution at 310 K. E_{vib} and E_{rot} were transferred into reactant momenta and displacements from equilibrium Cartesian coordinates. Reactants were randomly rotated about their Euler angles.

Relative velocities were added to reactants in accord with E_{CM}.

Trajectories started at an initial center-of-mass distance of 8.0 Å and halted after the formation of a

cluster ion or when product separation exceeded 10.0 Å. The E_{CM} (0.5 eV) was low enough to allow for

complex formation in collisions, but it was not so low as to substantially increase trajectory integration

time. The impact parameters (b) was chosen randomly between 0 and b_{max} (4.5 Å, estimated from the

maximum collision cross section using the IMoS program[93, 94]). The on-the-fly energies and gradients

were calculated using the Hessian-based predictor-corrector integration algorithms[88] implemented in the

Gaussian software, with Hessians updated every five steps. The ωB97XD/6-31+G (d) level of theory was

chosen for the integration as it represents a good compromise between accuracy and computational cost

for IL dynamics.[37, 56, 95-97] The trajectory propagation step size was set at 0.25 amu$^{1/2}$·Bohr (equivalent to

a step size of 0.4 fsec in trajectory time) to ensure the conservation of energy and momentum.

3.3 DFT calculation of dissociation energies

Geometry optimization and energy calculations for reactants and fragments were conducted at the

ωB97XD/6-31+G(d,p) level of theory using Gaussian 16. Their Cartesian coordinates are provided in the

Supporting Information. Cluster ion dissociation enthalpies were calculated at 0 K and have taken into

account ZPEs (scaled by a factor of 0.975)[98] to allow for a direct comparison with the CID experimental

data. Reaction potential energy surfaces (PESs) were calculated at 298 K.

4   Results

4.1 Formation of HEHN cluster ions in the negative mode

A mass spectrum of the negatively charged HEHN cluster ions is depicted in Fig. 1. For visual

clarity, ion intensities in the m/z range above 700 are scaled by a factor of 10 and presented in blue;

however, the portion of these ions accounts for only 4% of the total ions detected in the experiment. Most

of the species can be grouped into three distinct series: $[(HEHN)_nNO_3]^-$ (n = 0 – 13),

$[(HEHN)_n(HNO_3)NO_3]^-$ (n = 0 – 2), and $[(HEHN)_n(NaNO_3)NO_3]^-$ (n = 0 – 10). Each series is associated

with the progression of HEHN. Out of the three series, $[(HEHN)_nNO_3]^-$ represents the dominating one

and presents the longest progression; but the intensity decays exponentially from n = 1 to 5, becoming

insignificant afterwards. $[(HEHN)_n(HNO_3)NO_3]^-$ represents the second most important series, albeit the

progression lasts only to n = 2. The assignment of the minor series $[(HEHN)_n(NaNO_3)NO_3]^-$ was

supported by the CID of $[(NaNO_3)NO_3]^-$ (*m/z* of 147), which yielded only $NO_3^- + NaNO_3$. Na^+ was also

detected in the positive charged HEHN clusters by our group[37] and others,[25] despite the source remaining
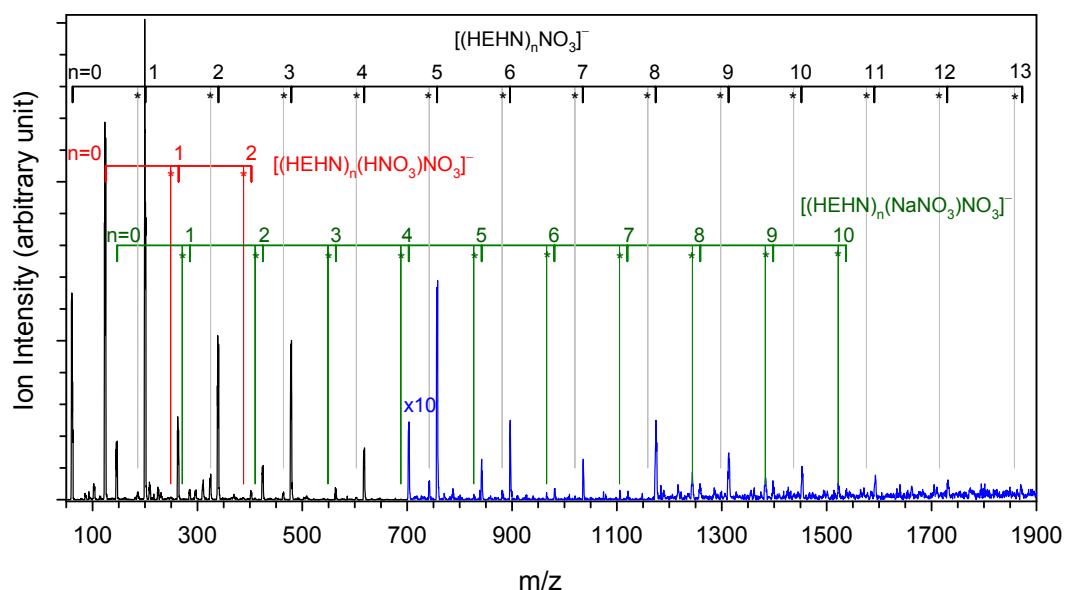
unknown.

Figure 1   Formation of negatively charged HEHN cluster ions when using 5 mM HEHN in acetonitrile/water (3:1). Ion intensities of *m/z* > 700 are scaled by a factor of 10.

Interestingly, we observed a group of species corresponding to a neutral mass loss of 15 from each

cluster ion in the three major series. These species are indicated by asterisks next to their parent ions.

The total fragment population is 5.5% in the series of $[(HEHN)_nNO_3]^-$ and in the series of

$[(HEHN)_n(HNO_3)NO_3]^-$, increases to 16.5% in the series of $[(HEHN)_n(NaNO_3)NO_3]^-$. The same mass 15

elimination was reported by Chambreau and co-workers before.[34] While they attributed the neutral

fragment to a $^\bullet CH_3$ radical, NH represents another possibility. The DFT-calculated activation barrier for

NH-elimination in HEHN is 4.52 eV. The elimination leads to a product-like complex first, which

ultimately dissociates to $HOCH_2CH_2NH_2 + NH$ at 4.73 eV. The acquisition of these amounts of

activation and dissociation energies was possible upon in-source collisional activation (i.e., within the

electric field between the end of the capillary and skimmer). Note the $[(HEHN)_n(NaNO_3)NO_3]^-$ series has

a higher NH-elimination probability than $[(HEHN)_nNO_3]^-$, which implies that the clusters containing

$NaNO_3$ weaken intra-cluster interaction. Also note that the in-source dissociation was observed in the

positively charged HEHN clusters before.[37] In the latter case, the dissociation was mediated by N_2H_4

elimination from a $[HE + H]^+$ moiety, producing $[(HE)_nC_2H_4OH]^+$ fragments in the $[(HE)_{n+1} + H]^+$ series.

4.2 Dissociation of $[(HEHN)_nNO_3]^-$

$[(HEHN)NO_3]^-$ (m/z 201). This ion not only represents the lightest HEHN cluster but also accounts for

26% of the total ion population in the negatively charged clusters. A tandem CID product ion mass

spectrum of $[(HEHN)NO_3]^-$, recorded at $E_{CM} = 3eV$, is presented in Fig. 2a. Product ions include

$[(HE)NO_3]^-$ at m/z 138 (which corresponds to HNO_3 elimination), $[(HNO_3)NO_3]^-$ at m/z 125

(corresponding to HE elimination), and NO_3^- at m/z 62 (corresponding to HEHN elimination).

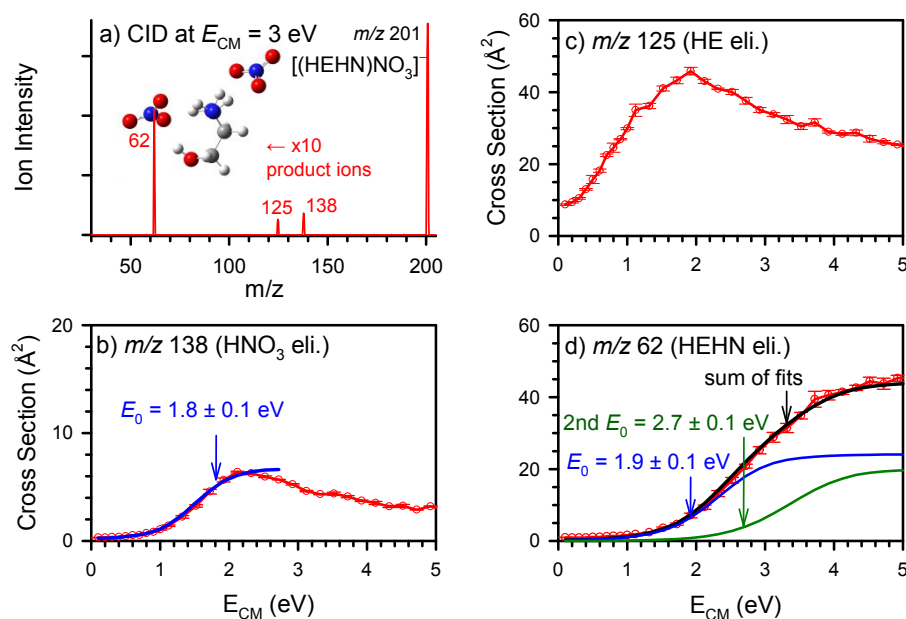**Figure 2** (a) Structure and a representative CID product ion mass spectrum for $[(HEHN)NO_3]^-$, wherein product ion intensities are scaled by a factor of 10; and (b – d) individual product ion cross sections as a function of E_{CM}, wherein the red lines with error bars represent the experimental data and the blue, green, and black lines represent the LOC fits.

Prior to the investigation of cluster dissociation mechanisms, GROMACS-based classical dynamics

simulations were conducted to explore the probable conformations of $[(HEHN)NO_3]^-$. In this pursuit,

100 candidate geometries were generated for optimization at the ωB97XD level using the 3-21G basis set. Geometries of low-energy conformations were re-optimized using 6-31G(d) and then 6-31+G(d,p). Nine different conformations were identified within the energy range of 0.06 eV, as presented in the order of relative enthalpy in Fig. S1 in the Supporting Information. In parallel, Venus-based direct dynamics simulations were executed to follow the reaction of HEHN + NO_3^- at the collision energy of 0.5 eV. Due to the extensive trajectory computing time (on average each trajectory took 240 CPU hours), we accumulated only 100 trajectories, most of which led to a complex. These complex structures were subjected to geometry optimization at the ωB97XD/6-31+G (d,p) level of theory. Remarkably, the Venus results were able to duplicate five conformations in Fig. S1, i.e., $[(HEHN)NO_3]^-$_a, c, e, g and h, and predicted the same global minimum conformation as GROMACS.

The two lowest-energy conformers, $[(HEHN)NO_3]^-$_a and b, differ in energy by less than 0.001 eV. The combination of the two accounts for a thermal Boltzmann population of 68%. They were used as the starting reactants in calculating the dissociation enthalpies for reactions 2b – d.

$[(HEHN)NO_3]^-$

$\rightarrow [(HE)NO_3]^- + HNO_3$	$\Delta H (0\ K) = 1.63\ eV$	(2b)
$\rightarrow [(HNO_3)NO_3]^- + HE$	$\Delta H (0\ K) = 1.20\ eV$	(2c)
$\rightarrow NO_3^- + HEHN$	$\Delta H (0\ K) = 1.80\ eV$	(2d.1)
$\rightarrow NO_3^- + HE + HNO_3$	$\Delta H (0\ K) = 2.59\ eV$	(2d.2)
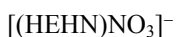
To probe the evolution of the HEHN moiety structure as well as the mechanisms for HE and HNO_3 elimination in $[(HEHN)NO_3]^-$, a static PES scan (without adding kinetic energy) was carried out along the center-of-mass separation between HEHN and NO_3^- using the ωB97XD/6-31G+(d,p) method. The PES is plotted in Fig. S2 in the Supporting Information, along with the changes of two H-bonds $r(HE\cdots H^+)$ and $r(H^+\cdots NO_3^-)$. As shown in Fig. S2a, the HEHN moiety adopts an ion-pair structure within the cluster and remains the ionic structure during the elimination of extra NO_3^-. However, it has the possibility of transitioning to a H-bonded neutral pair at the product asymptote, as one may expect from the trends of change in $r(HE\cdots H^+)$ and $r(H^+\cdots NO_3^-)$. Furthermore, the activation barrier for reverse proton transfer (PT)

within a single HEHN is only 0.02 eV – which can be easily overcome by collisional activation. In other words, there may exist a collisionally activated, product-like complex $[(HE)(HNO_3)NO_3]^-$. The fact that both HE and HNO_3 elimination was observed supports this hypothesis.
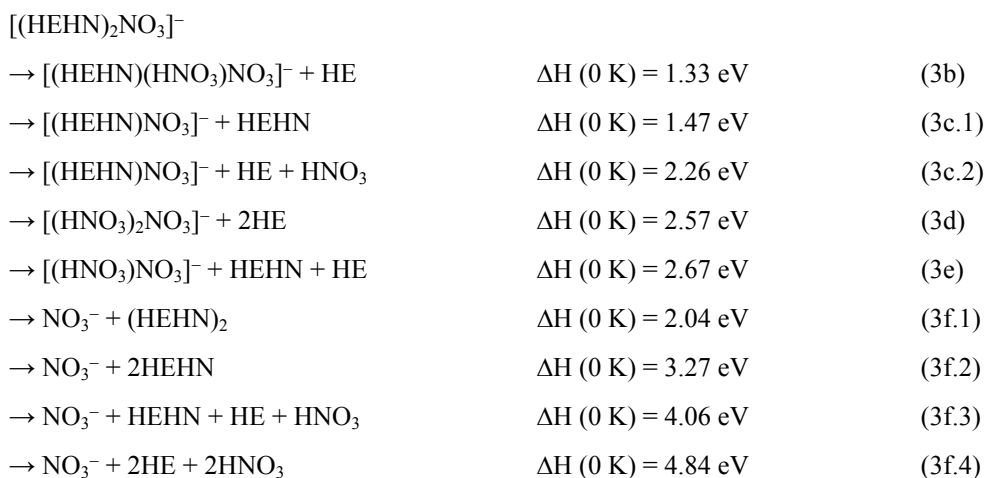
At E_{CM} below 3.0 eV, HE elimination represents the dominant dissociation mechanism for $[(HEHN)NO_3]^-$. The 0 K dissociation threshold for HE elimination is relatively low (1.20 eV), resulting in a non-zero cross section at the lowest experimental energy due to reactants internal energy and translational kinetic energy spread and Doppler broadening. For this reason, LOC fitting for the HE elimination cross sections was not feasible (the same reason applies to the product channels for other clusters which have non-zero cross sections at the lowest E_{CM}). The HNO_3 elimination cross section, on the other hand, declines (rather than levels off) at high energies. We attempted to fit the HNO_3 elimination only in the E_{CM} range of 0.05 – 2.7 eV. The testing fit allowed us to estimate an E_0 of 1.8 eV, close to the calculated ΔH (0K) of 1.63 eV.

There are noticeable decreases in the cross sections for both HNO_3 and HE elimination at E_{CM} above 2.0 eV. These are due to the competition with HEHN elimination at higher energies, as is evidenced by the fact that the sum of all product ion cross sections at high E_{CM} equals to the collision cross section of $[(HEHN)NO_3]^- + Xe$. The question arises as to whether the HEHN elimination were due to reaction 2d.1, 2d.2, or their combination. We first found that no satisfactory LOC fit could be obtained for the HEHN elimination cross section (Fig. 2d) using a single $\sigma(E_{CM})$ function. We therefore fitted the cross section using two sets of $\sigma(E_{CM})$ functions. E_0, n, and leveling off energy for each set were adjusted independently to reach the best fit for the cross section. As illustrated by the blue and green curves in Fig. 2d, the first LOC fit has $E_0 = 1.9$ eV, $n = 2.4$, and leveling off energy = 3.4 eV, and the second fit has $E_0 = 2.7$ eV, $n = 2.3$, and leveling off energy of 4.6 eV. The black curve represents the sum of the two fits. The results of LOC fitting have reinforced our hypothesis that there exist two cluster structures upon collisional activation and therefore two dissociation pathways. By comparing to the calculated ΔH (0 K), we conclude that the low-threshold, single HEHN elimination (i.e., reaction 2d.1) dominates throughout

the entire energy range, while the high-threshold, concomitant elimination of (HE + HNO_3) (i.e., reaction

2d.2) becomes important only at high energies. Our results reflect the reliability and robustness of the

threshold CID and the LOC simulation for dissociation energies.[99] As we may infer from the LOC fits in

Fig. 2d, the ratio of activated $[(HEH^+NO_3^-)NO_3]^-$ to $[(HE)(HNO_3)NO_3]^-$ is 5:4 at high energies.

$[(HEHN)_2NO_3]^-$ (*m/z* 340). The dissociation of $[(HEHN)_2NO_3]^-$ (Fig. 3a) resembles that of

$[(HEHN)NO_3]^-$ in terms of HE and HEHN elimination. The new features include elimination of 2HE,

2HEHN, and HEHN + HE; on the other hand, no single HNO_3 elimination was observed.

The combined approach of GROMACS classical dynamics simulations and DFT geometry

optimization was used to determine explicit cluster structures for $[(HEHN)_2NO_3]^-$. Four stable

conformations were identified within an energy range of 0.12 eV (see Fig. S3 in the Supporting

Information). The global-minimum conformer constitutes 82% of the thermal population and was

selected as the reactant structure to calculate the following dissociation enthalpies.

$[(HEHN)_2NO_3]^-$

$\rightarrow [(HEHN)(HNO_3)NO_3]^- + HE$	$\Delta H \ (0 \ K) = 1.33 \ eV$	(3b)
$\rightarrow [(HEHN)NO_3]^- + HEHN$	$\Delta H \ (0 \ K) = 1.47 \ eV$	(3c.1)
$\rightarrow [(HEHN)NO_3]^- + HE + HNO_3$	$\Delta H \ (0 \ K) = 2.26 \ eV$	(3c.2)
$\rightarrow [(HNO_3)_2NO_3]^- + 2HE$	$\Delta H \ (0 \ K) = 2.57 \ eV$	(3d)
$\rightarrow [(HNO_3)NO_3]^- + HEHN + HE$	$\Delta H \ (0 \ K) = 2.67 \ eV$	(3e)
$\rightarrow NO_3^- + (HEHN)_2$	$\Delta H \ (0 \ K) = 2.04 \ eV$	(3f.1)
$\rightarrow NO_3^- + 2HEHN$	$\Delta H \ (0 \ K) = 3.27 \ eV$	(3f.2)
$\rightarrow NO_3^- + HEHN + HE + HNO_3$	$\Delta H \ (0 \ K) = 4.06 \ eV$	(3f.3)
$\rightarrow NO_3^- + 2HE + 2HNO_3$	$\Delta H \ (0 \ K) = 4.84 \ eV$	(3f.4)

Since the cross sections for single HE and HEHN elimination (Fig. 3b – c) exceed zero at the lowest

E_{CM}, LOC fitting of their threshold profiles was not feasible. As aforementioned, there are two possible

pathways leading to HEHN elimination: either elimination of a single HEHN (i.e., neutral pair

evaporation[46]) as specified by reaction 3c.1 or concomitant elimination of separated HE + HNO_3 as

specified by reaction 3c.2. However, reaction 3c.2 has $\Delta H \ (0 \ K)$ at 2.26 eV, which is inconsistent with

the downward inflection for product ions *m/z* 201 around 1.6 eV and therefore could be ruled out.
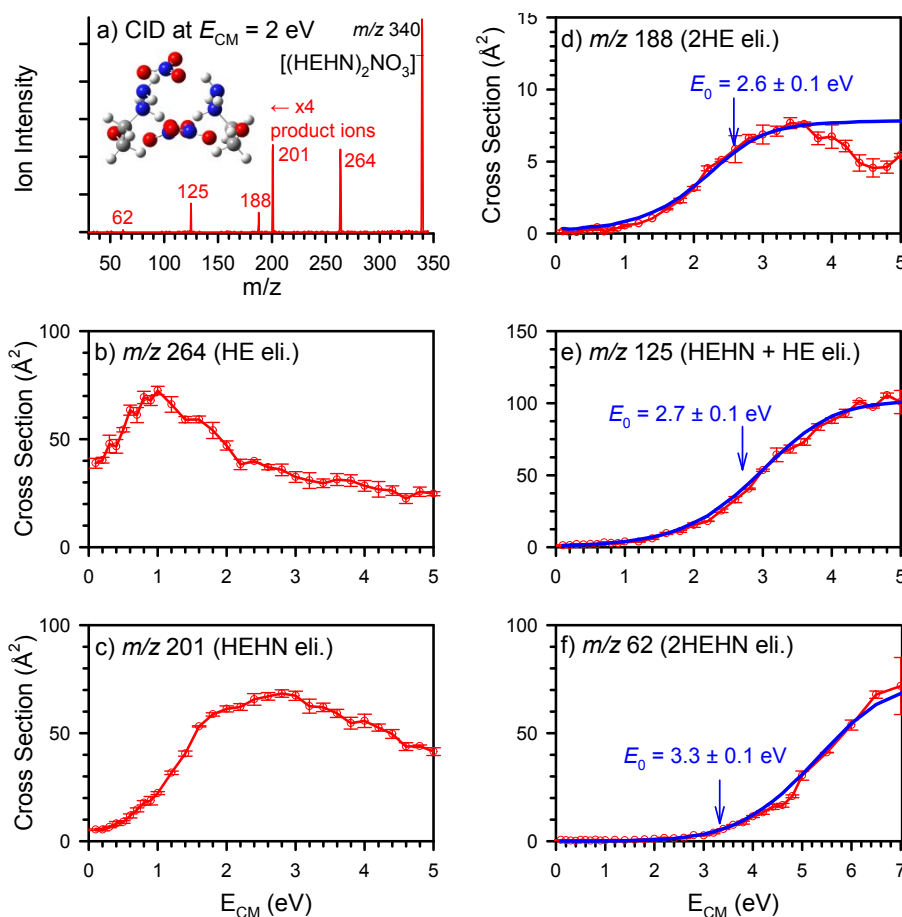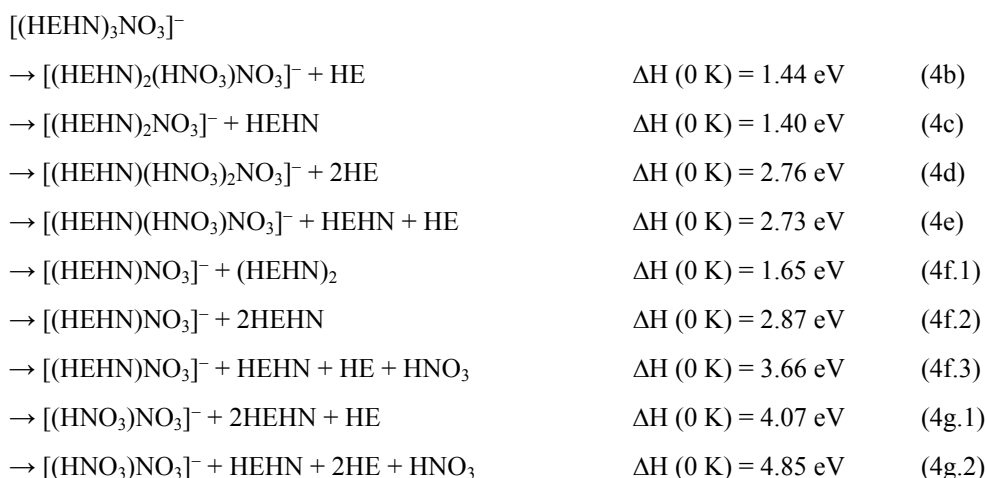
Figure 3   (a) Structure and a representative CID product ion mass spectrum for [(HEHN)$_2$NO$_3$]$^-$, wherein product ion intensities are scaled by a factor of 4; and (b – f) individual product ion cross sections as a function of E_{CM}, wherein the red lines with error bars represent the experimental data and the blue lines represent the LOC fits.

On the other hand, the LOC fitting was able to reproduce the cross sections for 2HE, (HEHN + HE), and 2HEHN elimination (Fig. 3d – f) over two orders of magnitude and from an energy below the threshold to 7 eV, except the decay of 2HE elimination at $E_{CM} > 3.6$ eV. The fitted experimental E_0 values have not only reached an excellent match with the calculated ΔH (0 K) for reactions 3d – e, but also determined the most probable pathway leading to NO$_3^-$ (*m/z* 62). Among the four proposed product channels 3f.1 – 4, the last two could be ruled out because both would require the experimentally excluded, single or double HNO$_3$ elimination. Reaction 3f.1 presents elimination of dimeric (HEHN)$_2$ with ΔH (0 K) at 2.04 eV; however, the corresponding low ΔH (0 K) does not fit to the relatively high-threshold profile in Fig. 3f. Consequently, reaction 3f.2 is the only possibility. The LOC fitted E_0 (3.3 eV) perfectly matches the calculated ΔH (0 K, 3.27 eV) for reaction 3f.2, indicating that this identification

is unambiguous.

[(HEHN)₃NO₃]⁻ (*m/z* 479). The CID results for $[(HEHN)_3NO_3]^-$, as well as the LOC fits to the

applicable product channels, are summarized in Fig. 4. Probable conformations of $[(HEHN)_3NO_3]^-$ are

provided in Fig. S4 in the Supporting Information. The fragmentation of $[(HEHN)_3NO_3]^-$ follows the

identical pattern as $[(HEHN)_2NO_3]^-$, including elimination of multiple HE and HEHN. But elimination of

single HNO_3 was not observed.

Using the lowest-energy and population-dominating (92%) conformer (i.e., $[(HEHN)_3NO_3]^-$_a in Fig.

S4) as the starting reactant, the dissociation enthalpies for various pathways were calculated as follows:

$[(HEHN)_3NO_3]^-$

$\rightarrow [(HEHN)_2(HNO_3)NO_3]^- + HE$	$\Delta H\ (0\ K) = 1.44\ eV$	(4b)
$\rightarrow [(HEHN)_2NO_3]^- + HEHN$	$\Delta H\ (0\ K) = 1.40\ eV$	(4c)
$\rightarrow [(HEHN)(HNO_3)_2NO_3]^- + 2HE$	$\Delta H\ (0\ K) = 2.76\ eV$	(4d)
$\rightarrow [(HEHN)(HNO_3)NO_3]^- + HEHN + HE$	$\Delta H\ (0\ K) = 2.73\ eV$	(4e)
$\rightarrow [(HEHN)NO_3]^- + (HEHN)_2$	$\Delta H\ (0\ K) = 1.65\ eV$	(4f.1)
$\rightarrow [(HEHN)NO_3]^- + 2HEHN$	$\Delta H\ (0\ K) = 2.87\ eV$	(4f.2)
$\rightarrow [(HEHN)NO_3]^- + HEHN + HE + HNO_3$	$\Delta H\ (0\ K) = 3.66\ eV$	(4f.3)
$\rightarrow [(HNO_3)NO_3]^- + 2HEHN + HE$	$\Delta H\ (0\ K) = 4.07\ eV$	(4g.1)
$\rightarrow [(HNO_3)NO_3]^- + HEHN + 2HE + HNO_3$	$\Delta H\ (0\ K) = 4.85\ eV$	(4g.2)

The significant cross sections for the HE elimination and HEHN elimination at the lowest

experimental energy align with the relatively low $\Delta H\ (0\ K)$ calculated for reactions 4b − c. The two cross

sections decrease dramatically at high energies due to the increasing elimination of (HEHN + HE),

reaction 4e. It is interesting to note that elimination of 2HE, reaction 4d, has an extremely low cross

section (Fig. 4d). The same phenomenon was observed in the dissociation of $[(HEHN)_2NO_3]^-$. The

implication is that the clusters have difficulty to accommodate reverse PT in more than one HEHN

moiety. The LOC fitting has reproduced the cross sections in Fig. 4e − f, and the resulting E_0 values

agree well with the DFT calculated $\Delta H\ (0\ K)$. Similar to the scenario for $[(HEHN)_2NO_3]^-$, the LOC

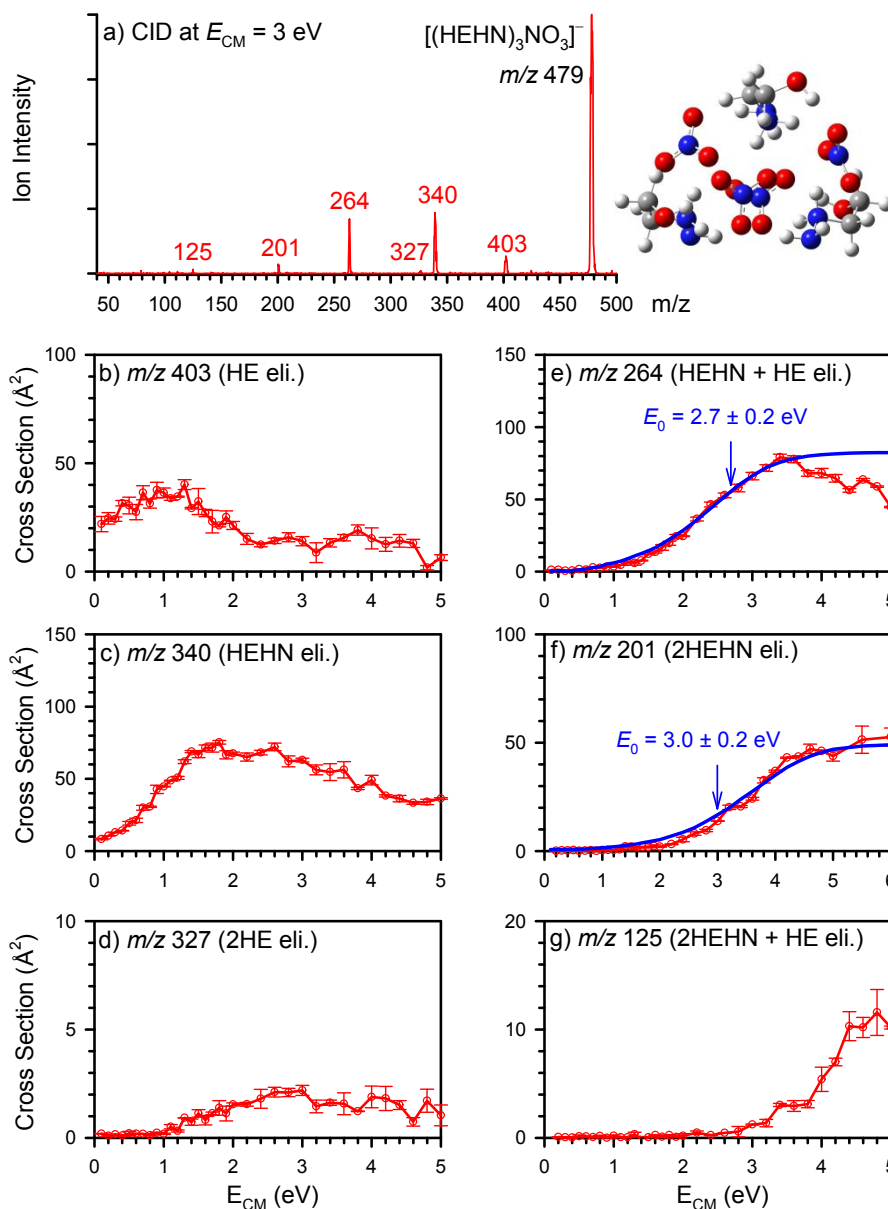fitting identified reaction 4f.2 as the most probable mechanism for simultaneous 2HEHN elimination.

Figure 4   (a) Structure and a representative CID product ion mass spectrum for $[(HEHN)_3NO_3]^-$; and (b – g) individual product ion cross sections as a function of E_{CM}, wherein the red lines with error bars represent the experimental data and the blue lines represent the LOC fit.

$[(HEHN)_{4-10}NO_3]^-$ (m/z 618, 757, 896, 1035, 1174, 1313, 1452). Figs. S5 – 7 in the Supporting

Information provide the CID results for each of $[(HEHN)_{4-6}NO_3]^-$. Because of the large cluster sizes, it

became difficult to calculate their probable conformations and identify dominating ones. Similar to their

low-mass analogues in the series, the CID of $[(HEHN)_{4-6}NO_3]^-$ is dominated by elimination of a single

HEHN at the low energy range (2 – 3 eV), which is outcompeted by elimination of simultaneous 2HEHN

at the medium energy range (4 – 6 eV) and by elimination of (2HEHN + HE) and/or 3HEHN at the high

energy range. Across the entire energy range, HE elimination remains as minor. This is the case when

HE appears either as the only neutral fragment or accompanied by the HEHN loss. It implies that reverse

PT becomes increasingly difficult in large cluster ions where each HEHN ion pair is surrounded by or

encapsulated within other ion pairs.

   Due to the significantly low intensities of the $[(HEHN)_{7-10}NO_3]^-$ cluster ions (less than 100

counts/sec), we were able to only measure their dissociation product ions (as depicted in Fig. S8 in the

Supporting Information) but not cross sections. Their major dissociation pathway corresponds to the

elimination of a single HEHN. The second major pathway leads to HE loss. The elimination of 2 – 3

HEHN moieties was also observed.

4.3 Dissociation of $[(HEHN)_n(HNO_3)NO_3]^-$

$[(HNO_3)NO_3]^-$ (m/z 125). This species "does not belong" to the HEHN clusters; nevertheless, both

$[(HNO_3)NO_3]^-$ and NO_3^- together accounts for one third of the total negative ions. The CID of

$[(HNO_3)NO_3]^-$ in Fig. 5 presents only the elimination of HNO_3. The LOC-fitted E_0 is close to the

calculated ΔH (0 K) for reaction 5.

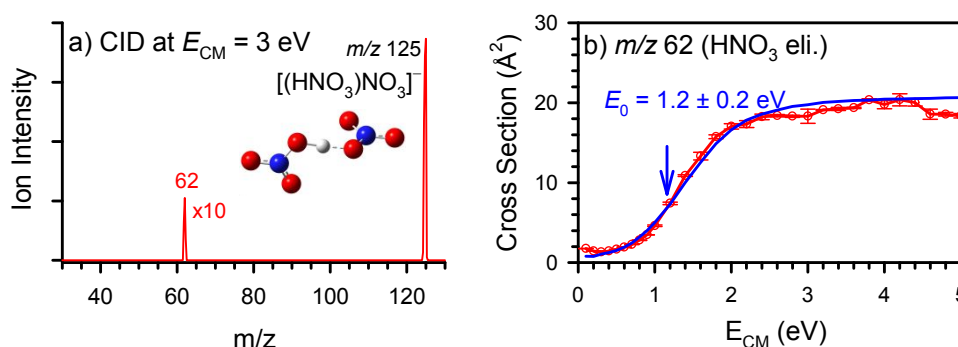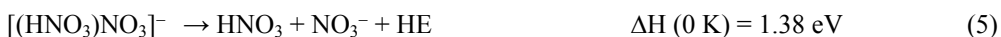$$[(HNO_3)NO_3]^- \rightarrow HNO_3 + NO_3^- + HE \qquad\qquad \Delta H \text{ (0 K)} = 1.38 \text{ eV} \qquad\qquad (5)$$

Figure 5   (a) Structure and a representative CID product ion mass spectrum for$[(HNO_3)NO_3]^-$, wherein product ion intensity is scaled by a factor of 10; and (b) product ion cross section as a function of E_{CM}, wherein the red line with error bars represents the experimental data and the blue line represents the LOC fit.

   $[(HEHN)_{1-2}(HNO_3)NO_3]^-$ (m/z 264 and 403). The probable conformations for these two clusters are

provided in Figs. S9 – 10 in the Supporting Information. For $[(HEHN)(HNO_3)NO_3]^-$, the lowest-energy

conformer represents a Boltzmann equilibrium population of 45%, while all the others have populations

ranging from a few percentage points to 22%. For $[(HEHN)_2(HNO_3)NO_3]^-$, the lowest-energy conformer

represents a Boltzmann equilibrium population of 75%. Therefore, their global-minimum conformations

were used as the initial structures for thermochemistry calculations. The fragmentation pathways for

$[(HEHN)(HNO_3)NO_3]^-$ and $[(HEHN)_2(HNO_3)NO_3]^-$ include the loss of HNO_3, HE (minor, only in

$[(HEHN)(HNO_3)NO_3]^-$), HEHN and HEHN + HNO_3, as shown in Fig. 6 and Fig. S11 in the Supporting

Information, respectively.

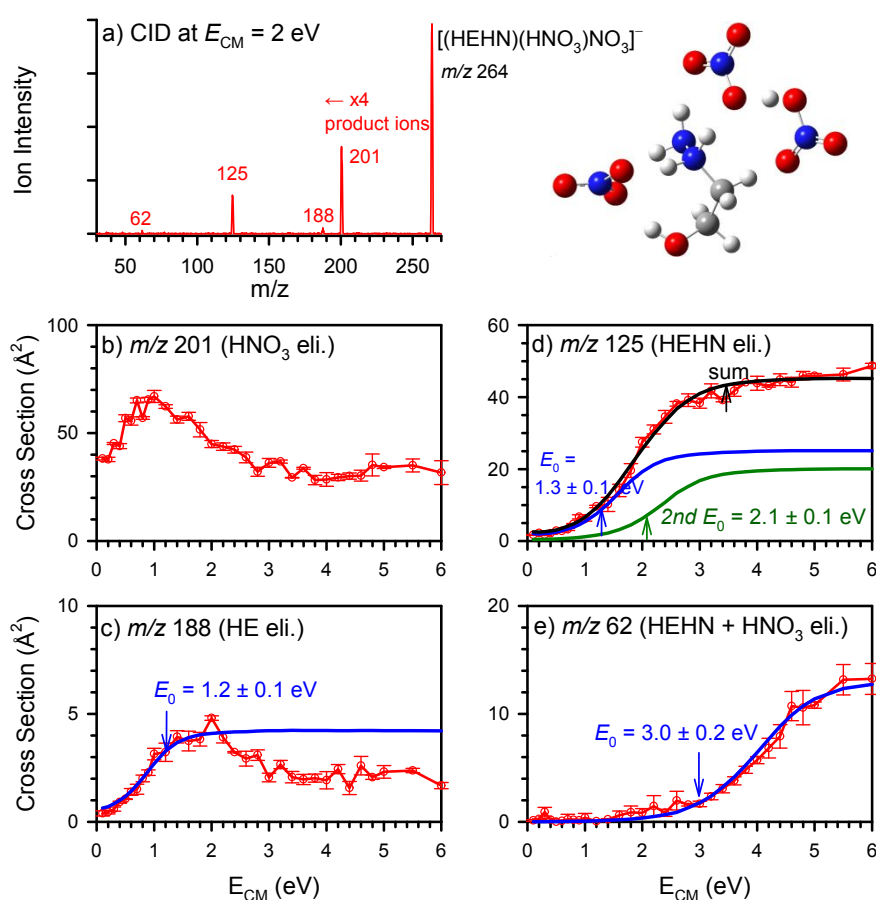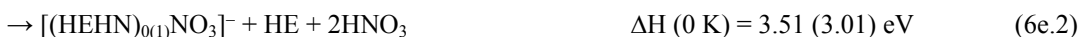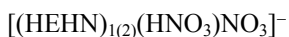**Figure 6**   (a) Structure and a representative CID product ion mass spectrum for $[(HEHN)(HNO_3)NO_3]^-$, wherein product ion intensities are scaled by a factor of 4; and (b – e) individual product ion cross sections as a function of E_{CM}, wherein red lines with error bars represent the experimental data and blue, green and black lines represents the LOC fits.

Their calculated dissociation enthalpies are as follows, wherein the values in parentheses refer to the

reactions of $[(HEHN)_2(HNO_3)NO_3]^-$:

$[(HEHN)_{1(2)}(HNO_3)NO_3]^-$

$\rightarrow [(HEHN)_{1(2)}NO_3]^- + HNO_3$ $\Delta H\ (0\ K) = 0.92\ (0.75)\ eV$ (6b)

$\rightarrow [(HEHN)_{0(1)}(HNO_3)_2NO_3]^- + HE$ $\Delta H\ (0\ K) = 1.24\ (1.33)\ eV$ (6c)

$\rightarrow [(HEHN)_{0(1)}(HNO_3)NO_3]^- + HEHN$ $\Delta H\ (0\ K) = 1.33\ (1.30)\ eV$ (6d.1)

$\rightarrow [(HEHN)_{0(1)}(HNO_3)NO_3]^- + HE + HNO_3$ $\Delta H\ (0\ K) = 2.12\ (2.08)\ eV$ (6d.2)

$\rightarrow [(HEHN)_{0(1)}NO_3]^- + HEHN + HNO_3$ $\Delta H\ (0\ K) = 2.72\ (2.22)\ eV$ (6e.1)

$\rightarrow [(HEHN)_{0(1)}NO_3]^- + HE + 2HNO_3$ $\Delta H\ (0\ K) = 3.51\ (3.01)\ eV$ (6e.2)

Since the intensity of $[(HEHN)_2(HNO_3)NO_3]^-$ was too low to allow for the measurement of individual product ion cross sections, the CID of $[(HEHN)(HNO_3)NO_3]^-$ in Fig. 6 was used to demonstrate their dissociation energy dependence. There appear to be good agreements between calculated dissociation enthalpies and experimental cross sections. The cross sections for HE and HNO_3 eliminations drop before reaching their calculated thresholds, indicating that HE and HNO_3 eliminations become less competitive at $E_{CM} \geq 2$ eV. The best LOC fitting of the product ions m/z 125 revealed two product channels, i.e., reactions 6d.1 and 2 with a ratio of 5:4 at high energies. The fitting of product ions m/z 62 identified reaction 6e.1 as the most probable mechanism.

5   Discussion

5.1 Ion compositions of different polarities

It is informative to examine and compare ion compositions in different charge modes. Positive clusters of HEHN were reported by Prince et al. using field evaporation of pure HEHN from an externally wetted titanium emitter [25] and by our lab using 5 mM HEHN in acetonitrile/water through a stainless steel capillary emitter.[37] Nearly identical cluster ion compositions and intensity distributions were observed in the two different studies. The series of positive clusters of HEHN is dominated by, in the order of importance, $[(HE)_{1-3} + H]^+$, $[(HEHN)_{1-2}HE + H]^+$, $[(HEHN)_{1-2}(HE)_2 + H]^+$, and $[(HE)_{0-2}C_2H_4OH]^+$ (where $C_2H_4OH^+$ was produced by dissociation of HEHN at the C−N bond).[25, 37]

Table 1 has compiled cluster ion populations detected in our positive and negative mass spectra. Groups of positive cluster ions are listed side by side with their counterparts in the negative mode. Overall, positive and negative cluster ions present well correlated compositions, such as $[HE + H]^+$ vs.

NO_3^-, $[(HE)_2 + H]^+$ vs. $[H(NO_3)_2]^-$, $[(HEHN)_{1-2}HE + H]^+$ vs. $[(HEHN)_{1-2}NO_3]^-$, and $[(HEHN)_{1-2}(HE)_2 +$

$H]^+$ vs. $[(HEHN)_{1-2}(HNO_3)NO_3]^-$. In terms of cluster m/z distributions, 99% of the positive ions are

populated within a m/z range $40 - 355$ while 80% of the negative ions are populated within m/z $62 - 340$.

Structurally, positive cluster ions are dominated by $[HE + H]^+$ (and its derivatives, total 53%) and the

short progressions of $[(HEHN)_{1-2}HE + H]^+$ (12.5%) and $[(HEHN)_{1-2}(HE)_2 + H]^+$ (2.2 %); negative ions are

featured by the long progressions of $[(HEHN)_{1-12}NO_3]^-$ (51.7%), in addition to NO_3^- (11.3%), $[H(NO_3)_2]^-$

(26.3)% and $[(HEHN)_{1-2}(HNO_3)NO_3]^-$ (5.1%).

Table 1   Cluster ion compositions in positive vs. negative ion modes

positive clusters[37]	(*m/z*)	ratio%	negative clusters	(*m/z*)	ratio%
$[HE + H]^+$	(77)	44.8	NO_3^-	(62)	11.3
$C_2H_4OH^+$ (= $[HE + H]^+ - N_2H_4$)	(45)	0.4			
$[HE + H]^+ - H_2O$	(59)	7.0			
$[(HE)Na]^+$		0.7			
$[(HE)_2Na]^+$		1.3	$[Na(NO_3)_2]^-$		3.4
$[(HE)_2 + H]^+$	(153)	27.6	$[(HNO_3)NO_3]^-$	(125)	20.7
$[(HE)C_2H_4OH]^+$	(121)	2.0			
$[(HE)_3 + H]^+$	(229)	1.5			
$[(HEHN)HE + H]^+$	(216)	4.0	$[(HEHN)NO_3]^-$	(201)	26.3
$[(HEHN)_2HE + H]^+$	(355)	8.5	$[(HEHN)_2NO_3]^-$	(340)	10.5
			$[(HEHN)_3NO_3]^-$		9.0
			$[(HEHN)_{4-12}NO_3]^-$		5.9
$[(HEHN)(HE)_2 + H]^+$		1.3	$[(HEHN)(HNO_3)NO_3]^-$		4.6
$[(HEHN)_2(HE)_2 + H]^+$		0.9	$[(HEHN)_2(HNO_3)NO_3]^-$		0.5
			$[(HEHN)_{1-9}(NaNO_3)NO_3]^-$		3.7
			Others		4.1

5.2 Fragmentation pathways and energies for clusters of different charges

Since the emitted cluster ions are mostly populated within the m/z range < 360 (regardless of charge

polarities), fragmentation of clusters within this m/z range is most relevant. Table 2 summarizes the

fragmentation pathways and threshold energies for these ions. Their neutral fragments consist of HEHN,

HE, HNO_3, and H_2O. Interestingly, the positive and negative cluster ions of similar m/z not only

eliminate neutral fragments of the similar (or the exact same) mass but also present the similar

dissociation energies for these neutral losses.

Table 2   Major dissociation pathways and energies in positive and negative cluster ions

positive clusters	fragments	ΔH (eV)	negative clusters	fragments	ΔH (eV)
$[(HE)_2 + H]^+$ $[CH_2CHNHNH_2 \cdot HE + H]^+ \cdot H_2O$ (m/z 153)	$[HE + H]^+ + HE$ $[HE + H]^+ + CH_2CH_2NHNH_2 + H_2O$	1.36 1.47	$[(HNO_3)NO_3]^-$ (m/z 125)	$NO_3^- + HNO_3$	1.38
$[(HEHN)HE + H]^+$ (m/z 216)	$[(HE)_2 + H]^+ + HNO_3$ $(HE + H)^+ + HEHN$	0.82 1.42	$[(HEHN)NO_3]^-$ (m/z 201)	$[(HNO_3)NO_3]^- + HE$ $NO_3^- + HEHN$	1.20 1.80
$[(HEHN)(HE)_2 + H]^+$ (m/z 292)	$[(HEHN)HE + H]^+ + HE$ $[(HE)_2 + H]^+ + HEHN$	1.06 1.09	$[(HEHN)(HNO_3)NO_3]^-$ (m/z 264)	$[(HEHN)NO_3]^- + HNO_3$ $[(HNO_3)NO_3]^- + HEHN$	0.92 1.33
$[(HEHN)_2HE + H]^+$ (m/z 355)	$[(HEHN)(HE)_2 + H]^+ + HNO_3$ $[(HE)_2 + H]^+ + HEHN + HNO_3$ $(HE + H)^+ + 2HEHN$	1.42 2.52 3.12	$[(HEHN)_2NO_3]^-$ (m/z 340)	$[(HEHN)(HNO_3)NO_3]^- + HE$ $[(HNO_3)NO_3]^- + HEHN + HE$ $NO_3^- + 2HEHN$	1.33 2.67 3.27

The similarities in their fragmentation behaviors may be better reflected in Scheme 1, in terms of primary and secondary dissociation channels of positive and negative clusters. The combination of Table 2 and Scheme 1 reveal the following points: 1) elimination of HE and HNO_3 represents the major dissociation channel for small clusters. HNO_3 elimination is facile only in small clusters that contain 1 – 2 HEHN moieties and/or extra HNO_3, but becomes less favorable in large clusters as HNO_3 is encapsulated within a large assembly and stabilized by NO_3^-; 2) elimination of HEHN dominates in large clusters (this is consistent with ion-pair evaporation from large cluster ions of other ILs);[46] and dissociation of single and double HEHN is slightly more facile in positive clusters (by 0.4 eV) than in negative ones; and 3) water elimination is a major dissociation channel in the positive clusters but absent in the negative ones (due to the lack of extra $[HE + H]^+$). Related to this, N_2H_4-elimination was observed in the positive ion source whereas NH-elimination was observed in the negative ion source.

Scheme 1   Fragmentation patterns in positive (red) vs. negative (green) HEHN cluster ions.

5.3 Cluster size dependence of dissociation energetics and intra-ion pair PT

The examination of HEHN and HE elimination enthalpies across the series of $[(HEHN)_nNO_3]^-$

provides further insight. Fig. 7a plots the precisely determined 0 K dissociation threshold energies based

on the combination of LOC fitted experimental E_0 and DFT calculated ΔH (0 K). Since we were not able

to obtain E_0 and ΔH (0 K) for every primary ion or every dissociation channel, another set of dissociation

energy dependence vs. cluster size data is presented in Fig. 7b using *apparent threshold energies*. The

apparent threshold energies were estimated by extending the tangents along the cross section rising sides

to zero. We may not directly compare the data set of actual vs. apparent dissociation thresholds, but both

sets present the same trends. The elimination energies of single and double HEHN decrease as the cluster

size increases; whereas the elimination energy of HE, either by itself or accompanying with HEHN,
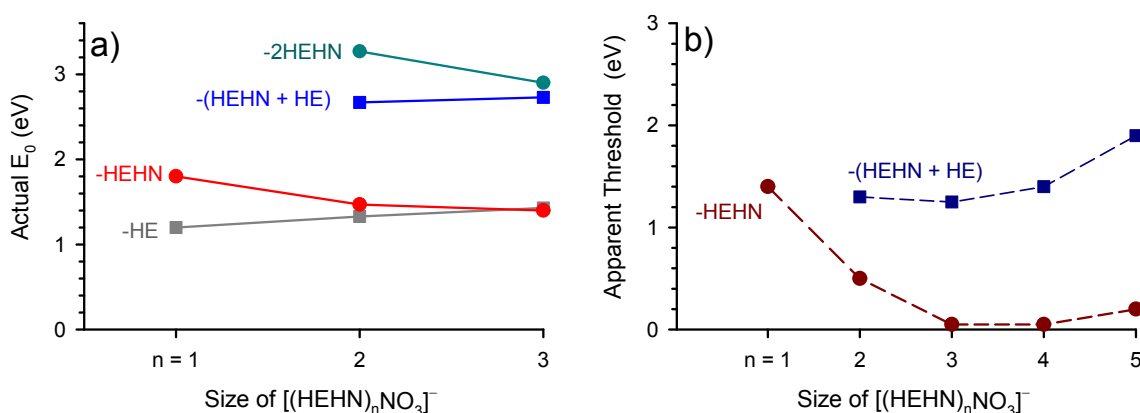
increases with the increasing size of the clusters.

Figure 7   Threshold energies for HE and HEHN elimination as a function of the $[(HEHN)_nNO_3]^-$ cluster size.

To address the opposite size dependence for HE and HEHN elimination, Fig. 8 compares the reverse

PT barrier for HEHN → HE·HNO$_3$ vs. the size/structure of host clusters. The barrier energetics was

acquired from relaxed PES scans along the PT coordinate in a monomer and the reverse PT coordinate in

a dimer. In the gas phase, a single HEHN monomer adopts a H-bonded HE·HNO$_3$ structure, but PT may

be triggered over a barrier of less than 0.02 eV (or slightly exothermic depending on the calculation levels

of theory). On the other hand, two dimeric structures may be considered, i.e., HE·HNO$_3$·HEH$^+$·NO$_3^-$ vs.

$(HEH^+ \cdot NO_3^-)_2$. The first structure is stable only at a center-of-mass separation of ≥ 9 Å between the two HEHN moieties. The barrier for reverse PT is 0.36 eV in $HE \cdot HNO_3 \cdot HEH^+ \cdot NO_3^-$ but increases to 0.51 eV in $(HEH^+ \cdot NO_3^-)_2$. The results support the findings in Fig. 7 that reverse PT becomes more unfavorable in the surrounding of HEHN ion-pair(s).

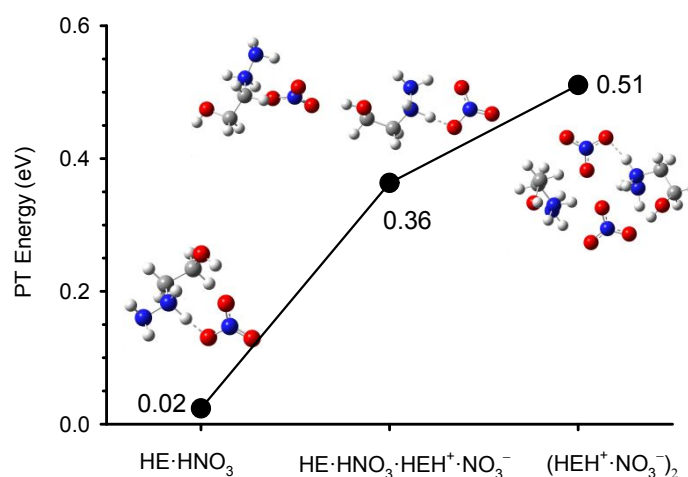**Figure 8**   Energy barrier for reverse proton transfer in different sizes and structures of $(HEHN)_{1-2}$, calculated at the ωB97XD/6-31+G(d,p) level of theory.

The same trend was observed for the PT-mediated HNO_3 elimination in the positive cluster ions,[37] i.e., ΔH (0K) is 0.82 eV for $[(HEHN)HE + H]^+ \rightarrow [(HE)_2 + H]^+ + HNO_3$ vs. 1.42 eV for $[(HEHN)_2HE + H]^+ \rightarrow [(HEHN)(HE)_2 + H]^+ + HNO_3$, and 0.83 eV for $[(HEHN)(HE)_2 + H]^+ \rightarrow [(HE)_3 + H]^+ + HNO_3$ vs. no HNO_3 elimination for $[(HEHN)_2(HE)_2 + H]^+$. This observation is consistent with previous vibrational predissociation spectrum of corresponding D_2-tagged $(HEH^+)_2NO_3^-$ clusters,[36] wherein the observed strong, red-shifted feature at ~2310 cm^{-1} was assigned to the frustrated intermolecular PT of the acidic proton on the secondary amino group to the NO_3^- species in this cluster, while no feature was seen in the D_2-tagged $(HEH^+)_3(NO_3^-)_2$ cluster (which here corresponds to the $[(HEHN)_2HE + H]^+$ cluster above[37]). The spectrum of the latter in this region resembled that of the bulk condensed phase simulated by ab initio molecular dynamics. Furthermore, the trend in Fig. 8 will reach an asymptotic value for the PT barrier in the liquid phase $(HEHN_{(l)} \rightarrow HNO_{3(l)} + HE_{(l)})$.

6   Conclusions

Experimental and computational works are presented toward understanding the chemistry of the 2-hydroxyethylhydrazinium nitrate clusters in different charge states. Mass spectrometry measurements were made to identify cluster ion compositions and to determine their dissociation product branching ratios, dissociation threshold energies, and dissociation rates (= cross section × relative velocity). These results were precisely matched to the explicit structures of primary cluster ions and fragments calculated using the combination of dynamics simulations and density functional theory. The major cluster ions formed in the negative charge state consist of $[(HEHN)_n(HNO_3)_{0-1}NO_3]^-$, the majority of which are populated within the m/z range of $62 - 340$. Fragmentation of these cluster ions is dominated by loss of neutral HEHN, HE, and HNO_3, of which the elimination of HE and HNO_3 require intra-ion pair proton transfer in the protic HEHN moiety and becomes difficult when the cluster size increases. Neutral loss results in an even narrower and lighter m/z distributions of cluster ions. These findings provide better knowledge of the various HEHN cluster stabilities and reaction thermodynamics. Comparisons to cluster formation and fragmentation in the positive charge state has revealed remarkable resemblances in terms of their similarities in m/z distributions, correlated compositions, fragmentation patterns, and threshold energies.

The existence of clusters is a defining feature of many ILs, playing a crucial role in IL-involved reactions and catalytic processes. This work highlights the distinctive IL clustering behaviors and micro-structures in the gas phase. The work has specially addressed the dominating ion-pair units within protic IL clusters at the molecular level, the intrinsic, solvent-free strengths of intra-ion pair electrostatic attraction, hydrogen bonding and the resulting intra-ion pair proton transfer. These interactions influence the assembly and evolution of clusters, as well as the mechanisms, kinetics, and dynamics of cluster breakup. These findings not only enhances our understanding of IL chemistry but also guides the design and applications of ILs.

Supporting Information

Conformations and Cartesian coordinates for cluster ions, PES for $[(HEHN)NO_3]^-$, and CID mass spectra for large clusters.

Data Availability

Acknowledgements

References

1   D. R. MacFarlane, M. Kar and J. M. Pringle, *Fundamentals of Ionic Liquids: From Chemistry to Applications*, Wiley‑VCH Verlag GmbH & Co. KGaA, Weinheim, Germany, 2017.
2   J. P. Hallett and T. Welton, *Chem. Rev.*, 2011, **111**, 3508-3576.
3   D. A. Fort, R. C. Remsing, R. P. Swatloski, P. Moyna, G. Moyna and R. D. Rogers, *Green Chem.*, 2007, **9**, 63-69.
4   W. M. Reichert, J. D. Holbrey, K. B. Vigour, T. D. Morgan, G. A. Broker and R. D. Rogers, *Chem. Commun.*, 2006, 4767-4779.
5   A. Avid, J. L. Ochoa, Y. Huang, Y. Liu, P. Atanassov and I. V. Zenyuk, *Nat. Comm.*, 2022, **13**, 6349.
6   H. Qi, Y. Ren, S. Guo, Y. Wang, S. Li, Y. Hu and F. Yan, *ACS Appl. Mater. Interfaces*, 2020, **12**, 591-600.
7   S. K. Shukla, S. G. Khokarale, T. Q. Bui and J.-P. T. Mikkola, *Front. Mater.*, 2019, **6**, 42.
8   X. Jin, L. Yu, D. Garcia, R. X. Ren and X. Zeng, *Anal. Chem.*, 2006, **78**, 6980-6989.
9   W. Gu, H. Chen, Y.-C. Tung, J.-C. Meiners and S. Takayama, *Appl. Phys. Lett.*, 2007, **90**, 033505.
10 K. Lunstroot, K. Driesen, P. Nockemann, C. Görller-Walrand, K. Binnemans, S. Bellayer, J. Le Bideau and A. Vioux, *Chem. Mater.*, 2006, **18**, 5711-5715.
11 A. Hammerl, G. Holl, M. Kaiser, T. M. Klapotke, R. Kranzle and M. Vogt, *Z. Anorg. Allg. Chem.*, 2002, **628**, 322-325.
12 M. Smiglak, A. Metlen and R. D. Rogers, *Acc. Chem. Res.*, 2007, **40**, 1182-1192.
13 S. Schneider, T. Hawkins, M. Rosander, G. Vaghjiani, S. Chambreau and G. Drake, *Energy Fuels*, 2008, **22**, 2871-2872.
14 S. Schneider, T. Hawkins, Y. Ahmed, M. Rosander, L. Hudgens and J. Mills, *Angew. Chem. Int. Ed.*, 2011, **50**, 5886-5888.
15 Y. Zhang and J. M. Shreeve, *Angew. Chem. Int. Ed.*, 2011, **50**, 935-937.
16 Q. Zhang and J. M. Shreeve, *Chem. Rev.*, 2014, **114**, 10527-10574.
17 P. D. McCrary, G. Chatel, S. A. Alaniz, O. A. Cojocaru, P. A. Beasley, L. A. Flores, S. P. Kelley, P. S. Barber and R. D. Rogers, *Energy Fuels*, 2014, **28**, 3460-3473.
18 R. Amrousse, T. Katsumi, N. Azuma and K. Hori, *Combust. Flame*, 2017, **176**, 334-348.
19 F. C. Gozzo, L. S. Santos, R. Augusti, C. S. Consorti, J. Dupont and M. N. Eberlin, *Chem. Eur. J.*, 2004, **10**, 6187-6193.
20 P. J. Dyson, I. Khalaila, S. Luettgen, J. S. McIndoe and D. Zhao, *Chem. Commun.*, 2004, 2204-2205.
21 G. P. Jackson and D. C. Duckworth, *Chem. Commun.*, 2004, 522-523.
22 R. Bini, O. Bortolini, C. Chiappe, D. Pieraccini and T. Siciliano, *J. Phys. Chem. B*, 2007, **111**, 598-604.
23 A. M. Fernandes, J. A. P. Coutinho and I. M. Marrucho, *J. Mass Spectrom.*, 2009, **44**, 144-150.
24 Y. Fujiwara, N. Saito, H. Nonaka and S. Ichimura, *J. Appl. Phys.*, 2012, **111**, 064901.
25 B. D. Prince, B. A. Fritz and Y.-H. Chiu, in *Ionic liquids: Science and Applications (ACS Symp. Ser.)*, American Chemical Society, 2012, vol. 1117, pp. 27-49.
26 S. W. Miller, B. D. Prince, R. J. Bemish and J. L. Rovey, *J. Propul. Power*, 2014, **30**, 1701-1710.
27 D. Krejci, F. Mier-Hicks, R. Thomas, T. Haag and P. Lozano, *J. Spacecraft Rockets*, 2017, **54**, 447-458.

28 A. L. Patrick, K. M. Vogelhuber, B. D. Prince and C. J. Annesley, *J. Phys. Chem. A*, 2018, **122**, 1960-1966.

29 A. L. Patrick, *Rapid Commun. Mass Spectrom.*, 2020, **34**, e8587.

30 J. L. Shamshina, M. Smiglak, D. M. Drab, T. G. Parker, H. W. H. Dykes, Jr., R. Di Salvo, A. J. Reich and R. D. Rogers, *Chem. Commun.* , 2010, **46**, 8965-8967.

31 T. W. Hawkins, A. J. Brand and G. W. Drake. *USA Pat.,* 20140190598, 2014.

32 A. Chowdhury and S. T. Thynell, *Propellants, Explos., Pyrotech.*, 2010, **35**, 572-581.

33 A. A. Esparza, S. D. Chambreau, G. L. Vaghjiani and E. Shafirovich, *Combust. Flame*, 2020, **220**, 1-6.

34 S. D. Chambreau, D. M. Popolan-Vaida, O. Kostko, J. K. Lee, Z. Zhou, T. A. Brown, P. Jones, K. Shao, J. Zhang, G. L. Vaghjiani, R. N. Zare and S. R. Leone, *J. Phys. Chem. A*, 2022, **126**, 373-394.

35 B. D. Prince, C. J. Annesley, R. J. Bemish and S. Hunt, AIAA Propulsion and Energy 2019 Forum, Indianapolis, IN, 2019.

36 H. J. Zeng, T. Khuu, S. D. Chambreau, J. A. Boatz, G. L. Vaghjiani and M. A. Johnson, *J. Phys. Chem. A*, 2020, **124**, 10507-10516.

37 W. Zhou, J. Liu, S. D. Chambreau and G. L. Vaghjiani, *Phys. Chem. Chem. Phys.*, 2023, **25**, 17370-17384.

38 M. J. Wainwright, J. L. Rovey, S. W. Miller, B. D. Prince and S. P. Berg, *J. Propul. Power*, 2019, **35**, 922-929.

39 S. W. Miller, B. D. Prince, R. J. Bemish and J. Rovey, 52nd AIAA/SAE/ASEE Joint Propulsion Conference, Salt Lake City, UT, 2016.

40 D. A. Bonhommeau, R. Spezia and M.-P. Gaigeot, *J. Chem. Phys.*, 2012, **136**, 184503.

41 C. Miller and P. C. Lozano, 52nd AIAA/SAE/ASEE Joint Propulsion Conference, Salt Lake City, UT, 2016.

42 N. M. Uchizono, A. L. Collins, C. Marrese-Reading, S. M. Arestie, J. K. Ziemer and R. E. Wirz, *J. Appl. Phys.*, 2021, **130**, 143301.

43 N. M. Uchizono, C. Marrese-Reading, S. M. Arestie, A. L. Collins, J. K. Ziemer and R. E. Wirz, *Appl. Phys. Lett.*, 2022, **121**, 074103.

44 F. Mier-Hicks and P. C. Lozano, *J. Propul. Power*, 2017, **33**, 456-467.

45 M. Breddan, A. Collins and R. Wirz, The 36th International Electric Propulsion Conference, Vienna, Austria, 2019.

46 J. F. de la Mora, M. Genoni, L. J. Perez-Lorenzo and M. Cezairli, *J. Phys. Chem. A*, 2020, **124**, 2483-2496.

47 C. E. Miller and P. C. Lozano, *Appl. Phys. Lett.*, 2020, **116**, 254101.

48 N. Nuwal, V. A. Azevedo, M. R. Klosterman, S. Budaraju, D. A. Levin and J. L. Rovey, *J. Appl. Phys.*, 2021, **130**, 184903.

49 L. Su, J. Zhuo, H. Liu, Z. Yao, X. Xu and S. Li, *Fuel*, 2023, **335**, 126919.

50 G. J. Van Berkel and F. Zhou, *Anal. Chem.*, 1995, **67**, 2916-2923.

51 P. Lozano and M. Martínez-Sánchez, *J. Colloid Interface Sci.*, 2004, **280**, 149-154.

52 P. Lozano and M. Martínez-Sánchez, *J. Colloid Interface Sci.*, 2005, **282**, 415-421.

53 A. Bruno, M. Schroeder and P. C. Lozano, in *AIAA SCITECH 2022 Forum*, American Institute of Aeronautics and Astronautics, 2021.

54 L. Su, Z. Yao, J. Zhuo, H. Liu, H. Yan and S. Li, *Energy & Fuels*, 2023, **37**, 13218-13230.

55 Y. Fang and J. Liu, *J. Phys. Chem. A*, 2009, **113**, 11250-11261.

56 W. Zhou, J. Liu, S. D. Chambreau and G. L. Vaghjiani, *Phys. Chem. Chem. Phys.*, 2022, **24**, 14033-14043.

57 M. Yamashita and J. B. Fenn, *J. Phys. Chem.*, 1984, **88**, 4671-4675.

58 F. M. Wampler, A. T. Blades and P. Kebarle, *J. Am. Soc. Mass Spectrom.*, 1993, **4**, 289-295.

59 F. Liu, W. Lu, X. Yin and J. Liu, *J. Am. Soc. Mass Spectrom.*, 2016, **27**, 59-72.

60 S. K. Chowdhury, V. Katta and B. T. Chait, *Rapid Commun. Mass Spectrom.*, 1990, **4**, 81-87.

61 T. Kim, K. Tang, H. R. Udseth and R. D. Smith, *Anal. Chem.*, 2001, **73**, 4162-4170.

62 K. Tang, A. V. Tolmachev, E. Nikolaev, R. Zhang, M. E. Belov, H. R. Udseth and R. D. Smith, *Anal. Chem.*, 2002, **74**, 5431-5437.

63 R. M. Moision and P. B. Armentrout, *J. Am. Soc. Mass Spectrom.*, 2007, **18**, 1124-1134.

64 A. N. Krutchinsky, I. V. Chernushevich, V. L. Spicer, W. Ens and K. G. Standing, *J. Am. Soc. Mass Spectrom.*, 1998, **9**, 569-579.

65   D. J. Douglas and J. B. French, *J. Am. Mass Spectrom.*, 1992, **3**, 398-408.

66   P. B. Armentrout, *J. Am. Soc. Mass Spectrom.*, 2002, **13**, 419-434.

67   C. Rebick and R. D. Levine, *J. Chem. Phys.*, 1973, **58**, 3942-3952.

68   R. D. Levine and R. B. Bernstein, *Molecular Reaction Dynamics and Chemical Reactivity*, Oxford University Press, New York, 1987.

69   P. B. Armentrout, *Int. J. Mass Spectrom.*, 2000, **200**, 219-241.

70   J. Liu, B. van Devener and S. L. Anderson, *J. Chem. Phys.*, 2002, **116**, 5530-5543.

71   M. M. Moe, J. Benny, Y. Sun and J. Liu, *Phys. Chem. Chem. Phys.*, 2021, **23**, 9365-9380.

72   P. J. Chantry, *J. Chem. Phys.*, 1971, **55**, 2746-2759.

73   C. Lifshitz, R. L. C. Wu, T. O. Tiernan and D. T. Terwilliger, *J. Chem. Phys.*, 1978, **68**, 247-260.

74   M. B. Sowa-Resat, P. A. Hintz and S. L. Anderson, *J. Phys. Chem.*, 1995, **99**, 10736-10741.

75   Y. Sun, M. M. Moe and J. Liu, *Phys. Chem. Chem. Phys.*, 2020, **22**, 14875-14888.

76   K. M. Ervin and P. B. Armentrout, *J. Chem. Phys.*, 1985, **83**, 166-189.

77   M. T. Rodgers, K. M. Ervin and P. B. Armentrout, *J. Chem. Phys.*, 1997, **106**, 4499-4508.

78   R. A. Marcus, *J. Chem. Phys.*, 1952, **20**, 359-364.

79   M. J. Abraham, T. Murtola, R. Schulz, S. Páll, J. C. Smith, B. Hess and E. Lindahl, *SoftwareX*, 2015, **1-2**, 19-25.

80   S. Páll, A. Zhmurov, P. Bauer, M. Abraham, M. Lundborg, A. Gray, B. Hess and E. Lindahl, *J. Chem. Phys.*, 2020, **153**, 134110.

81   M. J. Frisch, G. W. Trucks, H. B. Schlegel, G. E. Scuseria, M. A. Robb, J. R. Cheeseman, G. Scalmani, V. Barone, G. A. Petersson, H. Nakatsuji, X. Li, M. Caricato, A. V. Marenich, J. Bloino, B. G. Janesko, R. Gomperts, B. Mennucci, H. P. Hratchian, J. V. Ortiz, A. F. Izmaylov, J. L. Sonnenberg, D. Williams-Young, F. Ding, F. Lipparini, F. Egidi, J. Goings, B. Peng, A. Petrone, T. Henderson, D. Ranasinghe, V. G. Zakrzewski, J. Gao, N. Rega, G. Zheng, W. Liang, M. Hada, M. Ehara, K. Toyota, R. Fukuda, J. Hasegawa, M. Ishida, T. Nakajima, Y. Honda, O. Kitao, H. Nakai, T. Vreven, K. Throssell, J. A. Montgomery Jr., J. E. Peralta, F. Ogliaro, M. J. Bearpark, J. J. Heyd, E. N. Brothers, K. N. Kudin, V. N. Staroverov, T. A. Keith, R. Kobayashi, J. Normand, K. Raghavachari, A. P. Rendell, J. C. Burant, S. S. Iyengar, J. Tomasi, M. Cossi, J. M. Millam, M. Klene, C. Adamo, R. Cammi, J. W. Ochterski, R. L. Martin, K. Morokuma, O. Farkas, J. B. Foresman and D. J. Fox, Gaussian 16 Gaussian, Inc., Wallingford, CT, 2016, vol. Rev. D.01.

82   T. Lu, Sobtop, Beijing Kein Research Center for Natural Sciences, Beijing, 2023, vol. 1.0.

83   O. Ghasemalizadeh, S. Khaleghian and S. Taheri, *Int. J. Adv. Res.*, 2016, **4**, 1668-1686.

84   W. Humphrey, A. Dalke and K. Schulten, *J. Molec. Graphics* 1996, **14**, 33-38.

85   K. K. Baldridge, M. S. Gordon, R. Steckler and D. G. Truhlar, *J. Phys. Chem.*, 1989, **93**, 5107-5119.

86   W. L. Hase, *Advances in Classical Trajectory Methods, Vol. 1: Intramolecular and Nonlinear Dynamics*, JAI, Greenwich, Conn., 1992.

87   K. Bolton, W. L. Hase and G. H. Peslherbe, in *Modern Methods for Multidimensional Dynamics Computations in Chemistry* ed. D. L. Thompson, World Scientific, Singapore, 1998, pp. 143-189.

88   V. Bakken, J. M. Millam and H. B. Schlegel, *J. Chem. Phys.*, 1999, **111**, 8773-8777.

89   L. Sun and William L. Hase, *Rev. Comput. Chem.*, 2003, **19**, 79-146.

90   X. Hu, W. L. Hase and T. Pirraglia, *J. Comput. Chem.*, 1991, **12**, 1014-1024.

91   W. L. Hase, K. Bolton, P. de Sainte Claire, R. J. Duchovic, X. Hu, A. Komornicki, G. Li, K. Lim, D. Lu, G. H. Peslherbe, K. Song, K. N. Swamy, S. R. Vande Linde, A. Varandas, H. Wang and R. J. Wolf, VENUS 99: A General Chemical Dynamics Computer Program, Texas Tech University Lubbock, TX, 1999.

92   G. H. Peslherbe, H. Wang and W. L. Hase, *Adv. Chem. Phys.*, 1999, **105**, 171-201.

93   C. Larriba and C. J. Hogan, Jr., *J. Comput. Phys.*, 2013, **251**, 344-363.

94   C. Larriba-Andaluz and C. J. Hogan, Jr., *J. Chem. Phys.*, 2014, **141**, 194107.

95   J. Liu, W. Zhou, S. D. Chambreau and G. L. Vaghjiani, *J. Phys. Chem. B*, 2019, **123**, 2956-2970.

96   J. Liu, W. Zhou, S. D. Chambreau and G. L. Vaghjiani, *J. Phys. Chem. B*, 2020, **124**, 4303-4325.

97   W. Zhou, J. Liu, S. D. Chambreau and G. L. Vaghjiani, *J. Phys. Chem. B*, 2020, **124**, 11175-11188.

98   I. M. Alecu, J. Zheng, Y. Zhao and D. G. Truhlar, *J. Chem. Theory Comput.*, 2010, **6**, 2872-2887.

99   E. Paenurk and P. Chen, *J. Phys. Chem. A*, 2023, **128**, 333-342.

Data Availability

The data supporting this article have been included as part of the Supplementary Information.